

Heat Transfer of Supercritical Carbon Dioxide in Printed Circuit Heat Exchanger Geometries

Alan Kruienga

Mark Anderson

University of Wisconsin,
Madison, WI 53711

Roma Fatima

Texas A&M University,
College Station, TX 77843

Michael Corradini

Aaron Towne

University of Wisconsin,
Madison, WI 53711

Devesh Ranjan

Texas A&M University,
College Station, TX 77843

The increasing importance of improving efficiency and reducing capital costs has led to significant work studying advanced Brayton cycles for high temperature energy conversion. Using compact, highly efficient, diffusion-bonded heat exchangers for the recuperators has been a noteworthy improvement in the design of advanced carbon dioxide Brayton cycles. These heat exchangers will operate near the pseudocritical point of carbon dioxide, making use of the drastic variation of the thermophysical properties. This paper focuses on the experimental measurements of heat transfer under cooling conditions, as well as pressure drop characteristics within a prototypic printed circuit heat exchanger. Studies utilize type-316 stainless steel, nine channel, semi-circular test section, and supercritical carbon dioxide serves as the working fluid throughout all experiments. The test section channels have a hydraulic diameter of 1.16 mm and a length of 0.5 m. The mini-channels are fabricated using current chemical etching technology, emulating techniques used in current diffusion-bonded printed circuit heat exchanger manufacturing. Local heat transfer values were determined using measured wall temperatures and heat fluxes over a large set of experimental parameters that varied system pressure, inlet temperature, and mass flux. Experimentally determined heat transfer coefficients and pressure drop data are compared to correlations and earlier data available in literature. Modeling predictions using the computational fluid dynamics (CFD) package FLUENT are included to supplement experimental data. All nine channels were modeled using known inlet conditions and measured wall temperatures as boundary conditions. The CFD results show excellent agreement in total heat removal for the near pseudocritical region, as well as regions where carbon dioxide is a high or low density fluid.

[DOI: 10.1115/1.4004252]

Introduction

Minimizing capital costs and increasing plant operation allows power to become more affordable. As traditional energy sources in the United States, such as coal, natural gas, and petroleum, continue to rise in price and become scarce, it is clear that we must employ alternative sources of energy to ensure affordable economic growth in the future. Solar, wind, and nuclear are among the leading alternative energy sources.

The Department of Energy's program for next generation nuclear reactors establishes and defines broad goals to help increase nuclear's role in national and global production of energy [1]. Several of these designs employ a liquid metal or molten salt as the moderator and primary coolant and, therefore, necessitate a secondary power conversion cycle.

The supercritical carbon dioxide (S-CO₂) Brayton cycle is one of the recommended power cycles for use with these potential reactors. This Brayton cycle uses CO₂ in a supercritical state, at pressures above the fluid's critical pressure. As single phase is maintained throughout the cycle, it significantly contributes to simplified plant design. In addition, one can take advantage of the high power densities inherent with supercritical power conversion cycles. Highly efficient power conversion (>40%) at moderate temperatures provides additional incentive for closely investigating these cycles.

Many of the cycle designs use a recuperator and a heat exchanger to pre-cool the S-CO₂ directly before the compressor. As the S-CO₂ decreases in temperature at a given pressure; the

thermophysical properties transition sharply at a specific temperature termed the pseudocritical temperature (T_{pc}). The pseudocritical temperature is so named, because it mimics the critical temperature, and exhibits a maximum in specific heat as illustrated in Figure 1.

Heat transfer augmentation and deterioration occur under certain conditions in this region of drastic property variations for the heating mode [2]. While much work investigating heat transfer in heating modes for supercritical fluids has been done, comparatively less work exists in the cooling mode; only a few experiments to date exist using pure CO₂ [3–9]. Many existing heat transfer correlations tend to capture qualitative effects, but quantitatively disagree with each other, especially in the near critical region [10]. This work strives to supplement current heat transfer and pressure drop databases, evaluate heat transfer and pressure drop correlations, benchmark current models, and explore prototypic heat exchanger designs.

Experimental Facilities

Figure 2 shows a schematic representation of the experimental apparatus used during the heat transfer and pressure drop investigations. The heat transfer facility consists of two loops: one loop for the recirculation of CO₂ and another for the heat exchanger test section. The CO₂ loop contains several critical components: the main pump for fluid flow, the inverter for pump control, and the HPLC pump used to control system pressure.

The main pump is a ChemPump (Model GCT-1.5K-20S), capable of flow rates up to 14 m³/h, dynamic head up to 15 m, and system pressures up to 20 MPa. The pump is used in conjunction with a throttle valve to generate flow to the test section. Once the

Contributed by the Heat Transfer Division of ASME for publication in the JOURNAL OF THERMAL SCIENCE AND ENGINEERING APPLICATIONS. Manuscript received May 11, 2010; final manuscript received May 17, 2011; published online August 10, 2011. Assoc. Editor: Bengt Sundén.

Thermophysical Property vs Temperature at Critical Pressure for CO₂

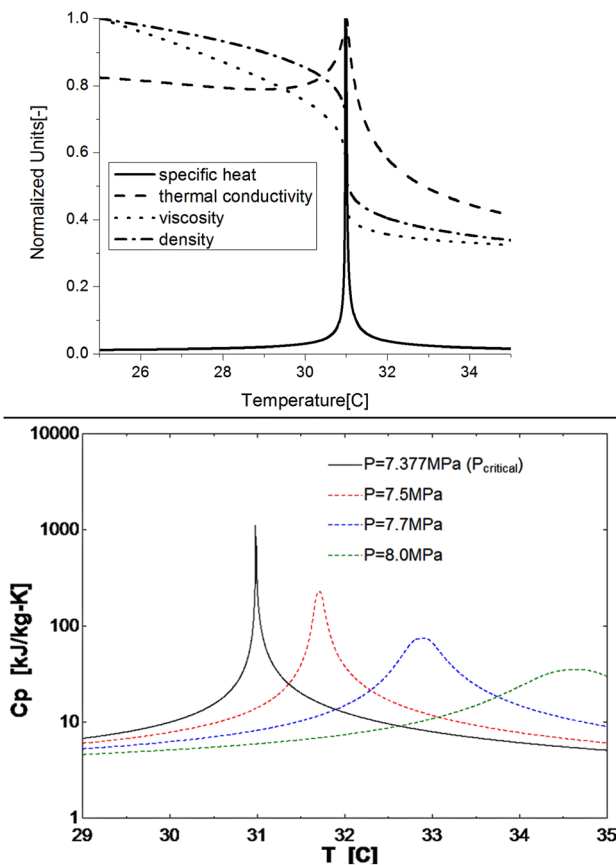


Fig. 1 Thermophysical property variations for CO₂ with both pressure and temperature. Maximum in specific heat represents pseudocritical temperature (T_{pc}). The critical pressure for carbon dioxide is 7.377 MPa.

throttle valve is set, the pump speed is varied to maintain a constant flow to the test section.

The pump speed is controlled with a Danfoss adjustable frequency inverter. The frequency inverter is controlled by a proportional-integral-derivative (PID) control scheme implemented in LABVIEW™ 8.5 [11]. This allows for the precise control of mass flow rates, ± 0.1 kg/h, during experiments. Loop conditions are monitored to provide feedback necessary for system stability.

Monitoring takes place using thermocouples and a pressure transducer. One K-type thermocouple monitors loop temperature (calibrated within 0.5 °C from 5 to 75 °C). The absolute pressure of the recirculation loop is monitored with a Siemens pressure transducer (Model 7MF4432-1GA10-1NC1-Z), and is recorded during experiments. The pressure transducer has operating limits of 0–40 MPa, with an accuracy of better than 0.1%. The pressure and temperature are monitored and controlled to ensure that the fluid density remains high enough to achieve the desired flow rates.

The system pressure is adjusted and controlled with a S-CO₂ pump capable of pumping CO₂ at pressures up to 60 MPa. A portable cooling bath, using water as the working fluid, is used to remove excess heat generated during experiments in the heat exchanger test loop.

The heat exchanger test loop consists of a Coriolis flow meter, heater, and test section. The flow rate is measured accurately with the Coriolis flow meter (Siemens Model 7ME4100-1DM11-1DA1), which has a maximum error of 0.3% for low flow conditions with typical errors of 0.1% of the measured value. The flow meter is placed before the heater to ensure cool CO₂ flows through it.

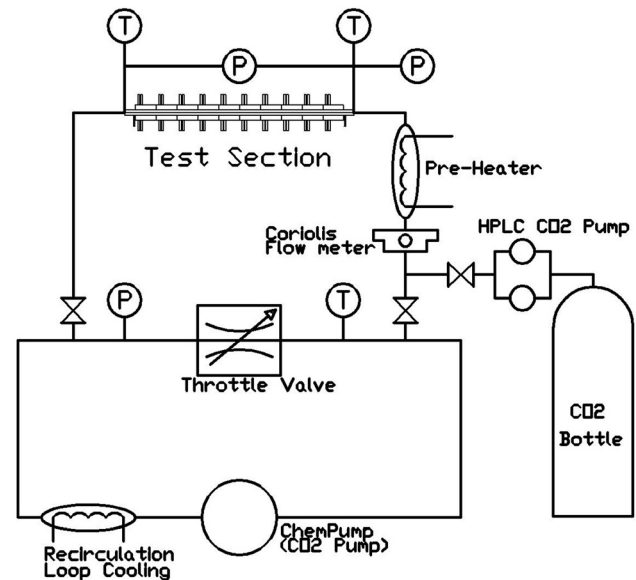


Fig. 2 Schematic of experimental facility at the University of Wisconsin

The test section consists of several pieces: the heat exchanger plate, the mating plate, and the cooling blocks. The heat exchanger plate is designed to be interchangeable with other prototypic designs, with flow paths fabricated by chemically etching into type 316 stainless steel. On each end of the plate, there are entrance and exit manifolds, with a distance from manifold to manifold of 500 mm. The channel configuration used in this study consists of nine semi-circular, parallel channels of 1.9 mm diameter. The heat exchanger plate is bolted to its mating plate to complete the prototypic heat exchanger (Fig. 3).

The mating plate consists of a flat plate with an O-ring groove machined into the surface, along with three holes at each end; two for thermocouples and one for a pressure tap. The O-ring is made from 1/16" Viton cord stock, cut to length, and glued together with Cyanoacrylate Adhesives to form the seal. In addition to the bolt holes in the mating plate and heat exchanger plate, a set of ten thermocouples are implanted into each plate.

Thermocouples measure the axial variation in wall temperature. Holes needed for the thermocouples, as shown in Fig. 4, have a large L/D ratio (~ 33), so electrical discharge machining was necessary. Each hole is 1 mm in diameter and 33 mm deep, spaced axially by 50 mm. Thermocouples are thermally coupled to the wall using 63/37 tin/lead solder as gap filler, due to 63/37's excellent thermal conductivity (40.9 W/m-K) and low melting point (183 °C).

Attached to the top of the mating plate and bottom heat exchanger plate are ten individual aluminum water blocks used to provide cooling, while also measuring local heat removal by performing an energy balance on each cooling block (Fig. 5). The

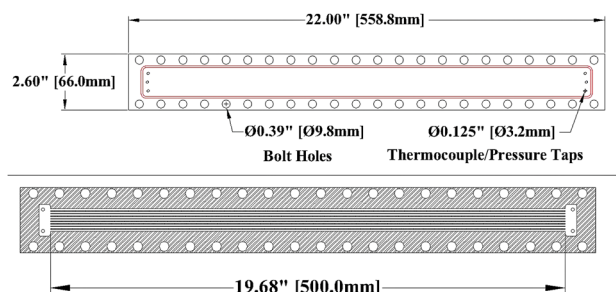


Fig. 3 Top and bottom of heat transfer test section

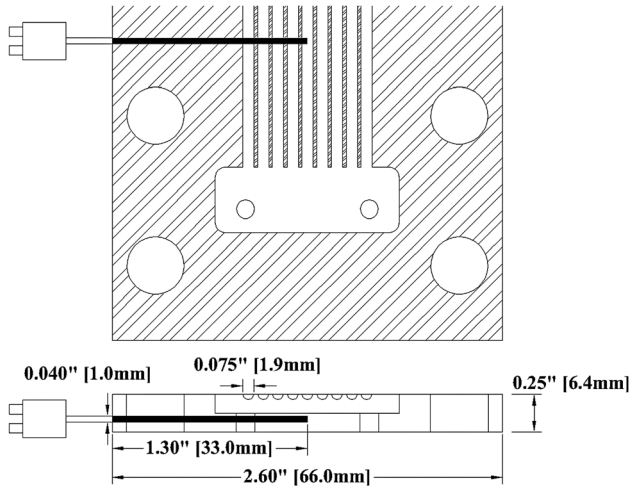


Fig. 4 Mixing manifold on test section. Also shown is the wall thermocouple implanted into the stainless steel.

inlet and outlet temperatures, and the volumetric flow rate of water for each cooling block are measured. Using these quantities, the local heat flux is calculated.

Data Reduction

One of the primary goals of this work is to obtain local heat transfer coefficients (HTCs) along the axial position of the test section. Prior to data reduction, it is necessary to ensure experiments are performed at steady state.

Experiments were found to be in steady state once the energy balance between the heat removed from the CO₂ was within 10% of the heat added to the cooling water. Heat for each fluid is calculated by the following equations:

$$Q_{CO_2} = \dot{m}(i_{in} - i_{out}) \quad (1)$$

$$Q_{H_2O} = \sum_{i=1}^{20} \dot{v}_i \rho_i C_{p-i} (T_{1-i} - T_{2-i}) \quad (2)$$

where \dot{m} is the mass flow rate of CO₂ and i is the inlet and outlet enthalpy, determined from the measured temperature and pressure. \dot{v}_i is the volumetric flow rate of the cooling water, ρ_i is the density, C_{p-i} the specific heat of water, and T is the inlet or outlet temperature of the water, where properties are determined by measured temperatures.

The local HTCs were obtained using values measured in each subsection, as illustrated in Fig. 6. Within each of the ten subsections, the local wall temperature and power removal are

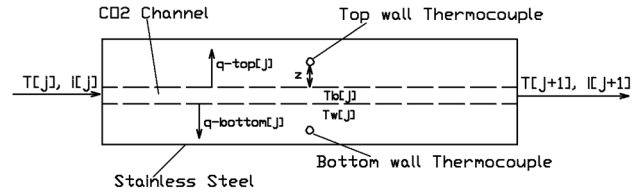


Fig. 6 One of the ten subsections for the test section

measured. An energy balance is employed to find the outlet enthalpy,

$$i_{CO_2}[j+1] = i_{CO_2}[j] - \frac{Q_j}{\dot{m}} \quad (3)$$

Using this balance, the temperature at $j+1$ is calculated and, therefore, the local bulk temperature is known for each subsection. The local wall temperature in contact with the fluid is calculated as expressed in the following:

$$T_w[j] = 0.5 \left(T_{top}[j] + \frac{q_{top}[j]z}{kA} + T_{bottom}[j] + \frac{q_{bottom}[j]z}{kA} \right) \quad (4)$$

where q is the power removal on the top or bottom cooling blocks (as indicated), k is the thermal conductivity of the stainless steel, A is the perpendicular area available for heat transfer, z is the distance between the thermocouple and the fluid, and T is the top or bottom temperature measured in the stainless wall.

The local HTC is then calculated, with the appropriate quantities known, by

$$h[j] = \frac{q_{top}[j] + q_{btm}[j]}{A_{tube}(T_b[j] - T_w[j])} \quad (5)$$

where A_{tube} is the area of the nine parallel channels over one subsection, which is 50 mm in length. All the HTC data shown will be derived from this analysis for local values.

Results

All experiments were performed at steady state conditions, which were found to be conditions when the heat balance between water and CO₂ was less than 10%, and after all temperatures (wall and fluid) were unchanging after 10 min. Data was taken at a rate of one point per second for 8 min. Then, all recorded values were averaged.

Heat Transfer

Several experiments were performed examining the effect of the bulk temperature on heat transfer. As shown in Fig. 8, which

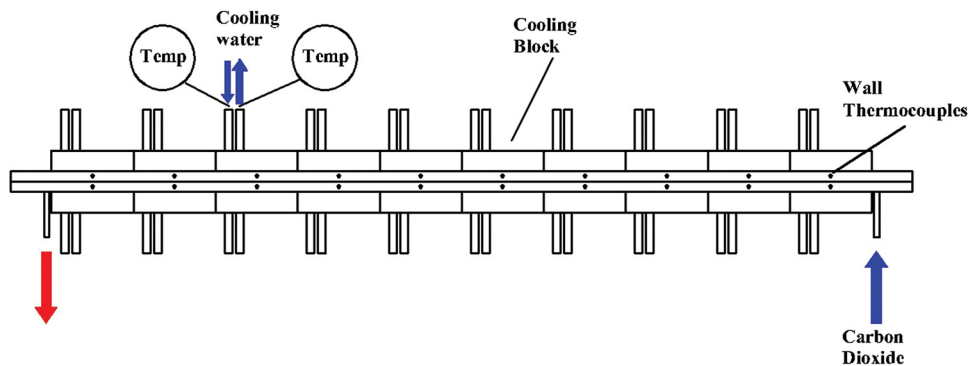


Fig. 5 Test section assembled with water cooling block

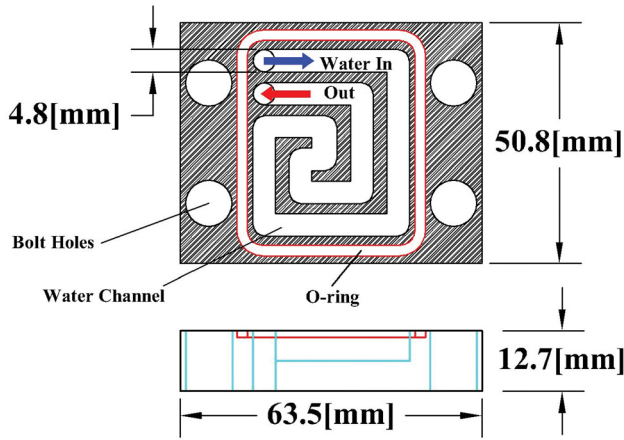


Fig. 7 Diagram of water cooling block. Each cooling block (20 in total) is bolted to the heat exchanger. Thermocouples to measure water temperature are placed at the inlet and outlet.

has constant inlet pressure and mass flow rate, inlet temperature significantly changes the heat transfer profile. Many previous S-CO₂ cooling mode studies failed to show bulk temperature and wall temperature [10], so this was an important consideration for this work. Literature shows that as the bulk temperature approaches T_{pc} the heat transfer increases rapidly [10]. This occurs due to the increasing specific heat of the fluid (Fig. 11). However, the peak in the heat transfer appears to occur slightly before the bulk temperature reaches T_{pc} (Fig. 9), which may indicate the importance of using a film temperature to predict the heat transfer. However, when considering error in the bulk temperature measurement, it is difficult to establish what the proper film temperature weighting should be between the wall and the bulk.

Previous investigations indicated that decreasing pressure, while remaining above the critical pressure, also increases the heat transfer [10]. This was found to occur, as represented in Fig. 10, which shows the heat transfer to increase with decreasing pressure, likely due to the increasing Prandtl number, as shown in Fig. 11. The Reynolds number is nearly equivalent over the normalized temperature span for the 7.5 and 8.1 MPa cases, which leaves the large variation in the Prandtl number driving the heat

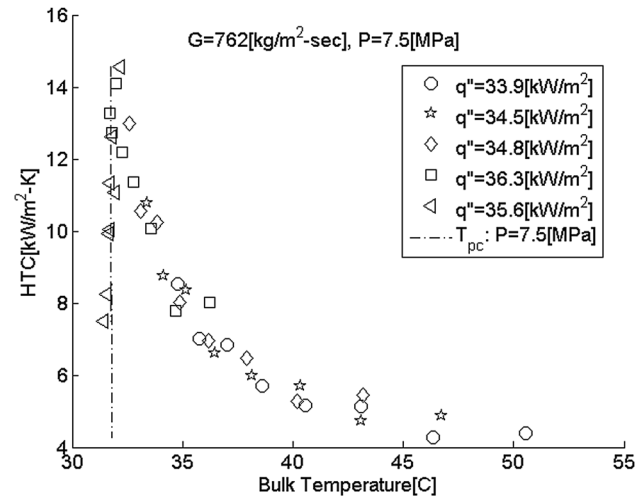


Fig. 9 Heat transfer coefficient as a function of bulk temperature

transfer coefficient peaks in the HTC. It should be noted that due to entrance and exit effects, resulting in heat transfer augmentation, the first and last axial locations were not plotted.

There has been some question as to what the most appropriate heat transfer correlation is for cooling. While many have been suggested, it is of interest to compare various correlations [10].

Established single phase correlations are suggested for supercritical fluids when temperature gradients are low within the flow [2]. One of the most widely used single phase correlation is Gnielinski's [12] given by

$$Nu_b = \frac{(f/8)(Re_b - 1000) Pr_b}{1 + 12.7\sqrt{(f/8)(Pr_b^{2/3} - 1)}} \quad (6)$$

where Re is the Reynolds number and Pr is the Prandtl number, both evaluated at bulk conditions, and f is the friction factor given by

$$f = \frac{1}{(0.79 \ln(Re) - 1.64)^2} \quad (7)$$

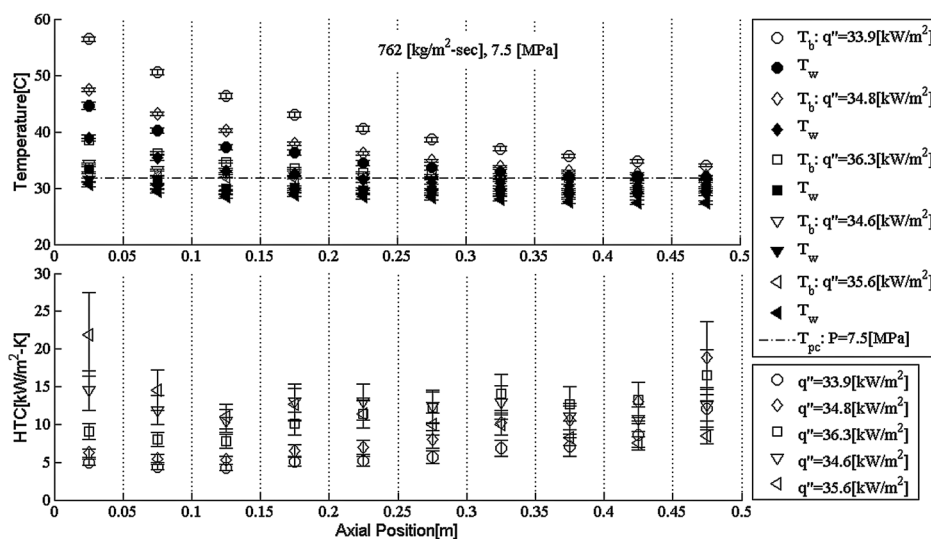


Fig. 8 Bulk and wall temperatures (top) for experiments with a mass flux of $762 \text{ kg/m}^2 \text{ s}$ and system pressure of 7.5 MPa. The bottom plot shows how the heat transfer coefficient changes as a function of length and inlet condition. Heat flux listed is the average heat flux over the test length.

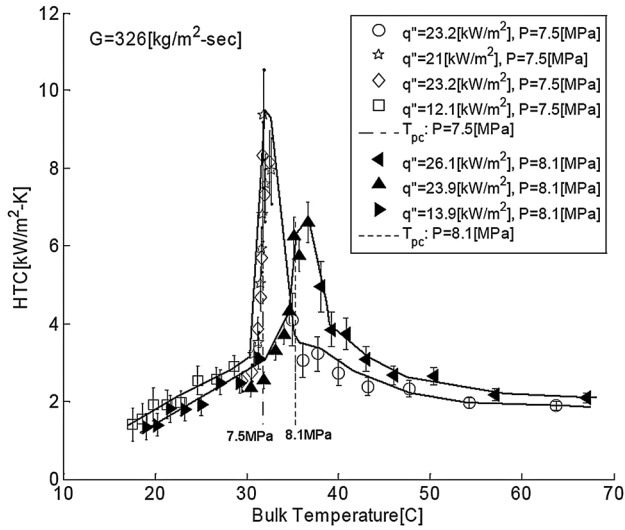


Fig. 10 Decreasing pressure results in significant increases in HTC

Through the Nusselt number the HTC can be calculated,

$$Nu_b = \frac{h d_{hyd}}{k_b} \quad (8)$$

where d_{hyd} is the hydraulic diameter and k_b is the thermal conductivity of CO_2 . Another widely accepted single phase correlation is the Dittus Boelter correlation [13], evaluated at the film temperature, which is defined below,

$$Nu_f = 0.023 Re_f^{0.8} Pr_f^{0.3} \quad (9)$$

$$T_f = \frac{T_b + T_w}{2} \quad (10)$$

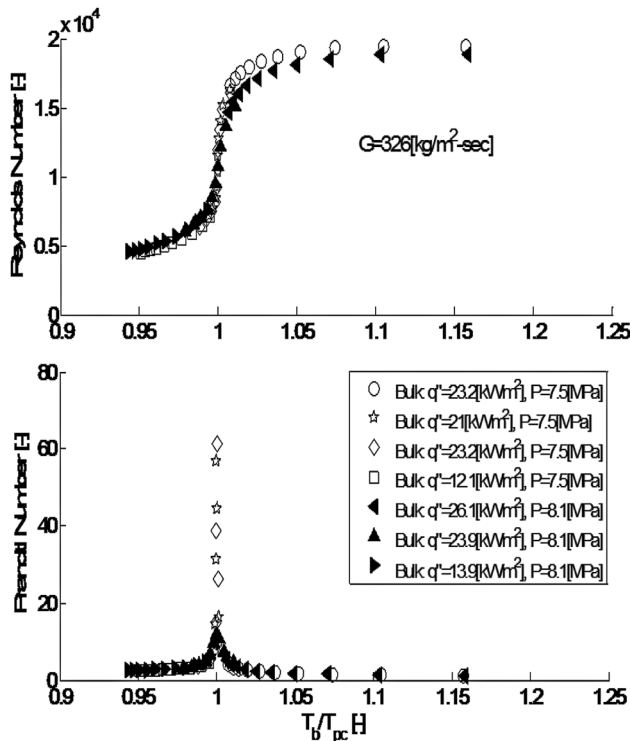


Fig. 11 Reynolds and Prandtl numbers evaluated under bulk conditions for low mass flux tests. Differences in HTC are due to changes in the Prandtl number.

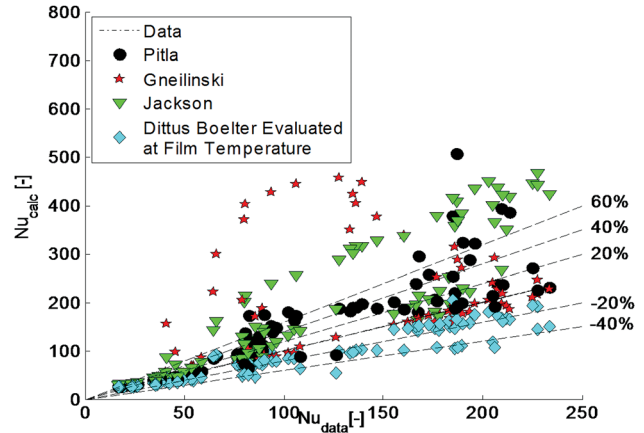


Fig. 12 Comparison of calculated Nusselt numbers to experimentally determined Nusselt numbers for several established correlations. Percentages indicate difference from a $y = x$ of 1.

A well known correlation used in supercritical fluids for the heating mode is the Jackson correlation [2], which corrects for the differences in temperature in the flow with variables evaluated at wall conditions,

$$Nu_b = 0.0183 Re_b^{0.82} Pr_b^{0.5} \left(\frac{\rho_w}{\rho_b} \right)^{0.3} \left(\frac{\bar{C}_p}{C_{p,b}} \right)^n \quad (11)$$

where n is based on

$$n = 0.4 \text{ for } T_b < T_w < T_{pc} \text{ or } 1.2 T_{pc} < T_b < T_w;$$

$$n = 0.4 + 0.2 \left(\frac{T_w}{T_{pc}} - 1 \right) \text{ for } T_b < T_{pc} < T_w;$$

$$n = 0.4 + 0.2 \left(\frac{T_w}{T_{pc}} - 1 \right) \left(1 - 5 \left[\frac{T_b}{T_{pc}} - 1 \right] \right) \text{ for } T_{pc} < T_b < 1.2 T_{pc} \text{ and } T_b < T_w;$$

The average specific heat is based on the enthalpy and temperature differences,

$$\bar{C}_p = \frac{i_w - i_b}{T_w - T_b} \quad (12)$$

There has been a recent correlation developed to predict in-tube cooling, where the Nusselt number is calculated at the wall and at bulk conditions using the Gnielinski correlation [14],

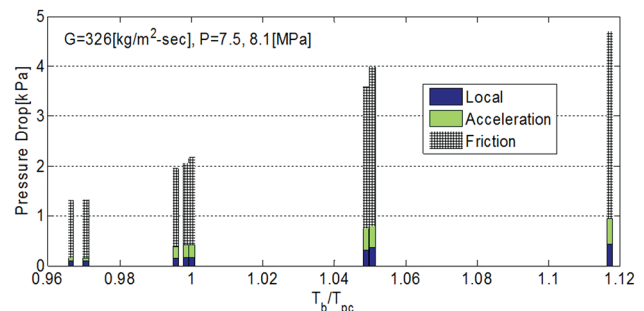


Fig. 13 Distribution of pressure losses between the local, acceleration, and frictional effects

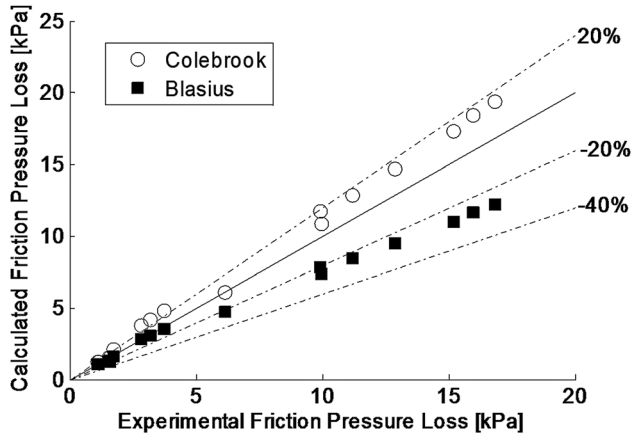


Fig. 14 Friction factors that include roughness slightly over predict the frictional pressure losses, while smooth tube friction factors under predict the experimental data

$$Nu_{Pitla} = \left(\frac{Nu_w + Nu_b}{2} \right) \frac{k_w}{k_b} \quad (13)$$

$$Nu_{Pitla} = \frac{h d_{hyd}}{k_b} \quad (14)$$

These correlations were evaluated for all experiments presented in the previous sections. It was found that the Gnielinski and Jackson correlations greatly over predicted the heat transfer at times, shown in Figure 12. The Pitla and Dittus Boelter correlations performed reasonably well. The Dittus Boelter consistently under predicted the expected heat transfer, while Pitla was slightly scattered at larger Nusselt numbers. This is an interesting result, and may warrant more investigation regarding which temperature (film, wall, or bulk) is of most importance for cooling heat transfer.

Pressure Loss

In supercritical fluid flows there are four main components of pressure drop [15]: frictional losses, acceleration losses, local losses, and gravitational losses. In this experiment there were no losses due to gravity, as the test section was in the horizontal configuration. The measured pressure losses are represented by the following equation:

$$\Delta P_{measured} = \Delta P_{friction} = \Delta P_{local} = \Delta P_{acceleration} \quad (15)$$

Local losses occurred at the entrance and exit due to the flow area differences from the mixing manifold to the small flow channels and were calculated by

$$\Delta P_{local} = \Delta P_{expansion} = \Delta P_{contraction} \quad (16)$$

$$\Delta P_{local} = \Delta P_{expansion} = \Delta P_{contraction} \quad (17)$$

$$\Delta P_{expansion} = \left[1 - \frac{A_{channels}}{A_{manifold}} \right]^2 \rho_{outlet} \frac{v_{outlet}^2}{2} \quad (17)$$

$$\Delta P_{contraction} = 0.5 \left[1 - \frac{A_{channels}}{A_{manifold}} \right]^{0.75} \rho_{in} \frac{v_{in}^2}{2} \quad (18)$$

where $A_{channels}$ is the cross sectional area of the channels, $A_{manifold}$ is the cross sectional area of the manifold, and v is the inlet and outlet fluid velocity. During most tests the local pressure drop is 5–8% of the total pressure drop (Figure 13).

Acceleration losses arose from the changing density throughout the flow and were more significant for tests near T_{pc} , as the density changed significantly in that region.

$$\Delta P_{accel} = G^2 \left[\frac{1}{\rho_{out}} - \frac{1}{\rho_{in}} \right] \quad (19)$$

where G is the mass flux of the CO_2 . This contribution to the total pressure drop varies depending on inlet and outlet conditions, especially when conditions are near T_{pc} .

The pressure drop due to friction was found to be the primary contributor to pressure loss (Fig. 13) and is defined as

$$\Delta P_{friction} = \frac{G^2 f L}{2 \rho_b d_{hyd}} \quad (20)$$

where L is the length of the test section, which is 500 mm.

For comparison, two correlations were investigated, one employing the smooth tube assumption and one using surface roughness. The Blasius correlation was chosen for the smooth tube correlation,

$$f_{Blasius} = \frac{0.316}{Re^{0.25}} \quad (21)$$

This correlation is valid for Reynolds numbers up to 10^5 .

The second correlation investigated is the Colebrook and White (CW), which accounts for surface roughness [16]. This equation is more complex than the Blasius solution, as the solution is implicit and must be calculated iteratively.

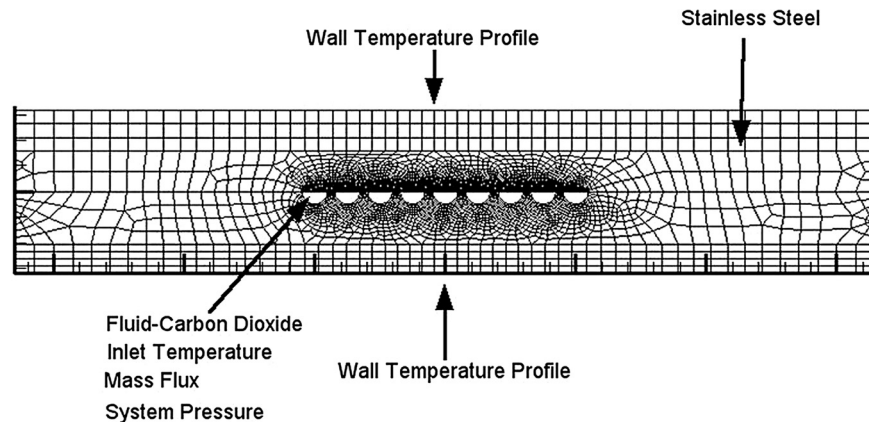


Fig. 15 End view of mesh used in CFD model. The model extends into the page 500 mm. The wall temperature boundary profile is a best fit polynomial of the experimentally measured temperature.

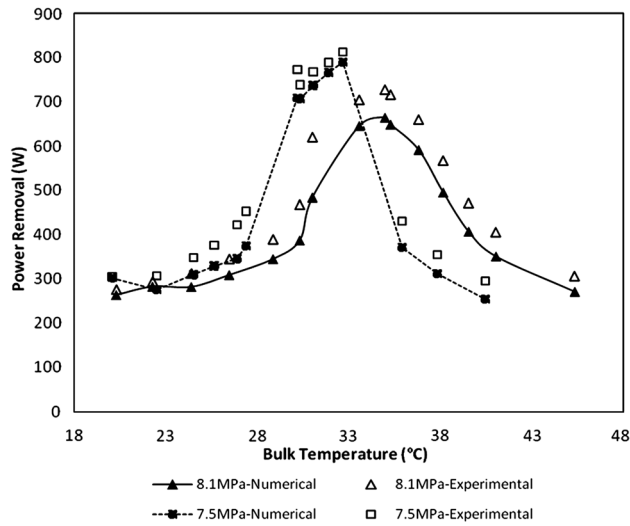


Fig. 16 Total power removal comparison versus average bulk temperature between experiment and CFD. Results show an excellent agreement between experiments and CFD.

$$f_{cw} = \left(-2 \log \left(\frac{\varepsilon/d}{3.7} + \frac{2.51}{\text{Re} \sqrt{f_{cw}}} \right) \right)^{-2} \quad (22)$$

ε/d is the surface roughness over hydraulic diameter, where ε was experimentally measured to be $7.4 \mu\text{m}$.

Figure 14 shows that for all the tests performed both the Blasius and CW well predict the frictional pressure drop below 5 kPa, while above that there is a divergence where the Blasius under predicts, and the CW slightly over predicts.

Computational Setup

The commercially available code, FLUENT 12.0 is employed to model the experimental setup described in the Experimental Facilities section above, using a 3D model with variable thermo-physical properties. The model was meshed in GAMBIT resulting in approximately 600,000 total cells. To resolve the properties at the boundaries of these channels, a finer mesh was used for the semi-circular channels and a coarser mesh for the bottom and the top plates. A fine mesh throughout the domain would have significantly increased the computational time. The upper, lower, and side boundaries of the domain were specified as wall boundary conditions.

All of the nine inlets were combined, as were the outlets of the channels, into single inlet and outlet boundary conditions. The inlet boundary condition was specified as mass flux. Simulations were carried out for pressure values of 7.5 MPa and 8.1 MPa, with different inlet fluid temperatures (ranging 25–50 °C). At the outlet of the channels, outflow/pressure boundary condition was specified depending upon the inlet temperature. As described in the experimental setup above, several thermocouples were used to measure the temperature of wall at different locations. A best fit curve from the experimentally measured wall temperature data was obtained (third order or fourth order polynomial), and used for initializing the wall temperature in the simulation. These temperature profiles were implemented in our simulations by making use of the user defined function (UDF). Figure 15 shows the end view of the mesh we used for the computational model.

To solve the mass, momentum, and energy equations, the pressure based solver was used for these simulations. The density based solver can also be used for this problem, but it takes longer to converge compared to the pressure based solver. Carbon dioxide at pseudocritical conditions was used as the fluid flowing through these channels. We extracted the properties of real carbon

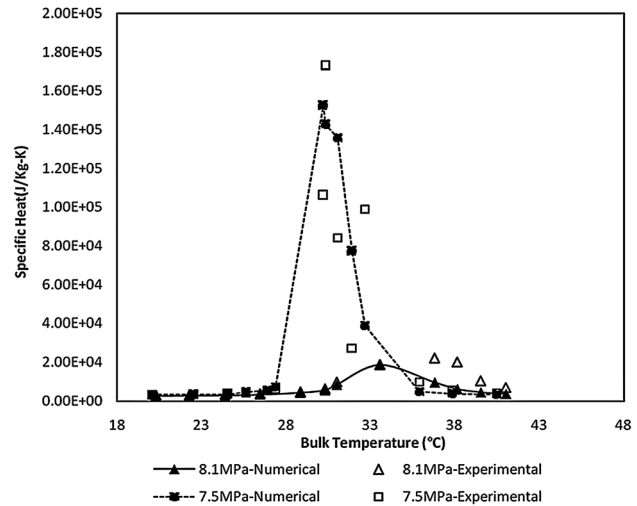


Fig. 17 Specific heat variation of carbon dioxide as a function of temperature at 7.5 and 8.1 MPa

dioxide gas by linking FLUENT with the National Institute of Standards and Technology database. The material used for the wall is stainless steel. The realizable $k - \varepsilon$ model with standard wall conditions was chosen to model turbulence in this simulation.

Figure 16 shows heat removal from the system for two different pressure conditions, at various bulk temperatures, for inlet mass flux of $762 \text{ kg/m}^2 \text{ s}$. The bulk temperature was defined as mean of inlet and outlet temperature.

It should be noted that the pseudocritical temperature for carbon dioxide at 7.5 MPa is 31.7°C , while at 8.1 MPa it is 35.2°C . One can clearly see that the heat removal curve peaks close to the pseudocritical point for both these scenarios. The peak was well captured in the simulation. Overall, the agreement between experiments and simulation is good. In both cases, if the temperature of the working fluid is increased above the pseudocritical temperature, there is a sudden deterioration in the heat removal from the system. This is not a surprising result, as one expects large thermophysical property changes near the pseudocritical point. This is well captured in the specific heat variation plot shown in Fig. 17. Both the experiments and simulations capture the spike in the specific heat around the pseudocritical point.

Conclusions

Experimental heat transfer results using S-CO₂ in the cooling mode were performed at conditions near the pseudocritical temperature. The results show a substantial heat transfer increase close to T_{pc} , which increases as the pressure is brought closer to the critical pressure. This is primarily caused by the increase in the Prandtl number.

Existing single phase correlations exhibit good agreement with heat transfer behavior, within 20% for experimental data, at conditions significantly above and below T_{pc} . However, near the T_{pc} region there is an over prediction by single phase correlations when the properties are evaluated at bulk conditions by more than 60% depending on the correlation. Replacing the bulk with the film temperature greatly improves the prediction of the HTC within 20–40%. Conditions under consideration were at pressures ranging from 7.5 to 8.1 MPa, mass flux ranges of $326\text{--}762 \text{ kg/m}^2 \text{ s}$, heat fluxes of $12\text{--}36 \text{ kW/m}^2$, and inlet temperature $20\text{--}100^\circ\text{C}$.

Frictional pressure drop is the primary contributor to the measured pressure loss, accounting for 80% or more of the total pressure losses. Established friction factors predict quite accurately the calculated frictional pressure losses and the importance of the surface roughness should be considered in these turbulent flows. Pressure losses due to acceleration account for $\sim 10\%$ of the total

losses for experiments near T_{pc} , due to the large density changes from inlet to outlet.

Computational modeling using commercially available software shows promising results for integral heat transfer. As a first basis of comparison the total power removal experimentally and computationally were compared and showed excellent agreement. Additional data reduction will compare the local HTC's to CFD simulations.

Future work in this study will compare several different prototypic heat exchanger designs, both experimentally and numerically, to evaluate the tradeoff between pressure drop and heat transfer.

Acknowledgment

Department of Energy Grant No. NEUP 09-777.
Department of Energy Grant No. DE-FG71D14776.
Qatar National Research Foundation Grant No. NPRP 08-494-2-193.

Nomenclature

T_{pc} = pseudocritical temperature
 C_p = specific heat (J/kg K)
HTC = heat transfer coefficient (W/m² K)
 i = enthalpy (J/kg)
 k = thermal conductivity (W/m K)
Pr = Prandtl number
Re = Reynolds number
 ρ = Density (kg/m³)
 \dot{v} = Volumetric flow rate (m³/s)
 \dot{m} = mass flow rate (kg/s)
 G = mass flux (kg/m² s)
 f = friction factor
 Q = heat removal (W)

Subscripts

b = bulk
f = film
w = wall

CO₂ = pertains to carbon dioxide

H₂O = pertains to water

References

- [1] U.S. DOE Nuclear Energy Research Advisory Committee, and Generation IV International Forum, 2002, "A Technology Roadmap for Generation IV Nuclear Energy Systems," GIF-002-00.
- [2] Jackson, J. D., and Hall, W. B., 1979, "Forced Convection Heat Transfer to Fluids at Supercritical Pressure," Institution of Mechanical Engineers, Conference Publications, **2**, pp. 563–611.
- [3] Huai, X. L., Koyama, S., and Zhao, T. S., 2005, "An Experimental Study of Flow and Heat Transfer of Supercritical Carbon Dioxide in Multi-Port Mini Channels Under Cooling Conditions," *Chem. Eng. Sci.*, **60**, pp. 3337–3345.
- [4] Dang, C., and Hihara, E., 2004, "In-Tube Cooling Heat Transfer of Supercritical Carbon Dioxide. Part 1. Experimental Measurement," *Int. J. Refrig.*, **27**(7), pp. 736–747.
- [5] Kuang, G., Ohadi, M. M., and Zhao, Y., 2004, "Experimental Study on Gas Cooling Heat Transfer for Supercritical CO₂ in Microchannel," Proceedings of the Second International Conference on Microchannels and Minichannels (ICMM2004), ASME, New York, pp. 325–332.
- [6] Liao, S. M., and Zhao, T. S., 2002, "Measurements of Heat Transfer Coefficients From Supercritical Carbon Dioxide Flowing in Horizontal Mini/Micro Channels," *Trans. ASME J. Heat Transfer*, **124**(3), pp. 413–420.
- [7] Son, C., and Park, S., 2006, "An Experimental Study on Heat Transfer and Pressure Drop Characteristics of Carbon Dioxide During Gas Cooling Process in a Horizontal Tube," *Int. J. Refrig.*, **29**(4), pp. 539–546.
- [8] Yoon, S. H., Kim, J. H., and Hwang, Y. W., 2003, "Heat Transfer and Pressure Drop Characteristics During the in-Tube Cooling Process of Carbon Dioxide in the Supercritical Region," *Int. J. Refrig.*, **26**(8), pp. 857–864.
- [9] Pettersen, J., Rieberer, R., Munkejord, S. T., 2000, "Heat Transfer and Pressure Drop for Flow of Supercritical and Subcritical CO₂ in Microchannel Tubes." Final Report for United States Army.
- [10] Cheng, L., Ribatski, G., and Thome, J. R., 2008, "Analysis of Supercritical CO₂ Cooling in Macro- and Micro-Channels," *Int. J. Refrig.*, **31**(8), pp. 1301–1316.
- [11] National Instruments, 2007, "Labview," **8.5**.
- [12] Kakaç, S., Shah, R. K., and Aung, W. C., 1987, *Handbook of Single-Phase Convective Heat Transfer*, Wiley, New York.
- [13] Dittus, W., and Boelter, L. M. K., 1930, *Heat Transfer in Automobile Radiators of the Tubular Type*, University of California, Publications in Engineering, **2**(13), pp. 443–461.
- [14] Pitla, S. S., Groll, E. A., and Ramadhyani, S., 2002, "New Correlation to Predict the Heat Transfer Coefficient During In-Tube Cooling of Turbulent Supercritical CO₂," *Int. J. Refrig.*, **25**(7), pp. 887–895.
- [15] Pioro, I. L., 2006, *Heat Transfer and Hydraulic Resistance at Supercritical Pressures in Power Engineering Applications*, ASME Press, New York, p. 334.
- [16] Colebrook, C. F., 1939, "Turbulent Flow in Pipes, With Particular Reference to Transition Region Between Smooth and Rough Pipe Laws," *Inst. Civ. Eng. London*, **12**(4), pp. 393–422.